Joule-Heating Synthesis of High-Entropy Oxide Nanoparticles as Sulfion Oxidation Catalysts for Efficient and Durable Hybrid Seawater Electrolysis

Weifeng Su, Tao-Jing Huang, Haoliang Huang, Zhipeng Yu, Fei Lin, Chenyue Zhang, Hao Tan, Kaiyang Xu, Run Ran, Weimian Zhang, Yaowen Xu, Chao Song, Guang-Jie Xia, Zuxin Chen,* and Lifeng Liu**

Direct seawater electrolysis for hydrogen production is hindered by high energy consumption and the competing chlorine evolution reaction (CER), which compromises efficiency and generates corrosive byproducts. Replacing oxygen evolution reaction (OER) with sulfion oxidation reaction (SOR) is promising to circumvent CER, but practical applications demand high-efficiency powdery, supported SOR catalysts operating at high current densities. Herein, we report the synthesis of FeCoNiMnCuO high-entropy oxide nanoparticles (HEO NPs) supported on carbon through an ultrafast Joule-heating method, which show outstanding SOR performance in natural seawater, achieving 500 mA cm^{-2} at 0.545 V versus the reversible hydrogen electrode and demonstrating stability over 100 h. *Operando* X-ray absorption spectroscopy and in-situ Raman spectroscopy studies reveal that in-situ formed metal sulfides, particularly Fe—S and Cu—S species, serve as active sites. Density functional theory calculations confirm the high-entropy effect lowers the energy cost of the potential-determining step by increasing intrinsic charge stability. Furthermore, a membrane electrode assembly incorporating the HEO catalysts operates stably at 500 mA cm^{-2} over 500 h with low energy consumption and no chlorine evolution, showcasing substantial potential for low-cost, energy-saving, and chlorine-free hydrogen production from seawater.

1. Introduction

Hydrogen (H_2) has emerged as a critical component in the global transition toward clean and sustainable energy systems. As a versatile clean energy carrier, H_2 can help decarbonize many sectors such as transportation, power generation, and domestic heating. In particular, it is a key enabler allowing for significant reduction of carbon dioxide in industrial processes that are hard to electrify, including steel making, synthetic fuels, and petrochemical manufacturing.[1,2] Among various H_2 production methods,[3,4] water electrolysis powered by renewable energy (e.g., solar, wind, geothermal and tidal waves) is now considered one of the most promising approaches to generating green H_2 and has therefore received considerable attention in the past decade.[5–8] For both alkaline water electrolysis (AWE) and proton exchange membrane water electrolysis (PEMWE) technologies currently commercially available in the market, it is typically mandatory to use high-purity freshwater as feedstocks.[9,10] However, as the global demand for H_2 increases, large-scale deployment of water electrolyzers is expected to consume vast amounts of freshwater. In many regions around the world, water scarcity is already a critical concern, and using freshwater for H_2 production may exacerbate this issue.[11] A promising and potentially cost-effective alternative is to develop direct seawater electrolysis (SWE)

W. Su, Z. Chen
School of Electronic Science and Engineering (School of Microelectronics)
South China Normal University
Foshan 528225, P. R. China
E-mail: chenzuxin@m.scnu.edu.cn

W. Su, H. Huang, F. Lin, C. Zhang, H. Tan, K. Xu, R. Ran, W. Zhang, Y. Xu, C. Song, L. Liu
Songshan Lake Materials Laboratory (SLAB)
Dongguan 523808, P. R. China
E-mail: liu.lifeng@sslab.org.cn

T.-J. Huang, G.-J. Xia
School of Physical Sciences
Great Bay University
Dongguan 523000, P. R. China
E-mail: xiagj@gbu.edu.cn

T.-J. Huang, G.-J. Xia
Center for Intelligent Computing
Great Bay Institute for Advanced Study
Dongguan 523000, P. R. China

Z. Yu
International Iberian Nanotechnology Laboratory (INL)
Avenida Mestre Jose Veiga, Braga 4715-330, Portugal

The ORCID identification number(s) for the author(s) of this article can be found under https://doi.org/10.1002/adfm.202506415

DOI: 10.1002/adfm.202506415

technology, considering that seawater accounts for ≈96.5% of the Earth's water reserves and renewable energy is widely available near coasts,[12] the combination of which is favorable for green H_2 production and its subsequent shipment to regions of demand.

Despite its potential, direct seawater electrolysis has been facing several technical challenges, such as high energy consumption and interference from impurity ions during anodic and cathodic reactions.[12–14] One of the major issues is the competing chlorine evolution reaction (CER) taking place at the anode, which not only compromises the energy efficiency, but also generates environmentally unfriendly and corrosive chlorine (Cl_2) or hypochlorite (ClO^-) species, posing significant challenges in terms of the durability of materials and components in electrolyzers.[15] To overcome these challenges, using thermodynamically more favorable anodic oxidation reaction (AOR) to replace the energy-demanding oxygen evolution reaction (OER) and notorious interfering CER has recently been explored,[16–19] which has already demonstrated to be able to substantially reduce the energy needed for electrolysis and effectively bypass the CER.[13] Among various AORs proposed so far,[20–23] the sulfion oxidation reaction (SOR) shows substantial promise for hybrid seawater electrolysis, because of the low theoretical oxidation potential (−0.48 V versus standard hydrogen electrode – SHE) and fast reaction kinetics of sulfide ions involving only two electrons ($S^{2-} \rightarrow S + 2e^-$).[24] Substitution of SOR for OER/CER not only completely prevents harmful chlorine chemistry from happening in SWE but can also markedly reduce the anodic potential at a given current density, thereby saving electrical energy.[25] Moreover, since the anodic products are soluble polysulfides and there aren't any gases generated at the anode, the explosion risk caused by H_2—O_2 crossover, like that possibly occurring in conventional alkaline electrolyzers, can be fully mitigated.[20,26] For these reasons, SOR-assisted SWE has recently attracted great interest from the research community. For instance, Zhang and co-workers reported energy-saving H_2 production in seawater by coupling SOR with hydrogen evolution reaction (HER) and realized a low cell voltage of 0.97 V and low electricity consumption of 2.32 kWh m^{-3} H_2 at 300 mA cm^{-2}.[25] Xiao et al. developed bifunctional Co_3S_4 nanowires on nickel foam that were used to catalyze both SOR and HER,[27] enabling SWE to be achieved at 100 mA cm^{-2} with a low power consumption of 1.185 kWh m^{-3} H_2. Lately, Yu and co-workers demonstrated that sulfur and phosphorus co-doped FeCoNiCrMn high-entropy alloy (HEA-SP) catalysts exhibited excellent electrocatalytic performance for SOR in alkaline-saline water.[28] Using HEA-SP as the anode catalyst and in the presence of a bipolar membrane (BPM), they significantly reduced the energy consumption to 0.253 kWh m^{-3} H_2 at 100 mA cm^{-2}. Notwithstanding some progress, most SOR catalysts reported so far were directly grown on nickel foam or other self-supporting substrates that are not easy to scale up for practical implementation (e.g., with areas of square meters).[29,30] Moreover, given the high reducibility, S^{2-} ions can very easily react with metal or alloy leading to the formation of brittle metal sulfides, especially at high current densities, which would result in the corrosion and pulverization of metal-based self-supporting substrates (e.g., nickel foam) and eventually the failure of the anode. Therefore, for real-world applications, it is highly preferable to develop highly dispersed, powdery electrocatalysts with improved SOR performance, because it is compatible with the present fabrication techniques of membrane electrode assemblies that can be readily scaled up. However, powdery SOR catalysts have been rarely reported by far.

In this work, we report the synthesis of high-entropy oxide nanoparticles (HEO NPs) comprising cheap transition metals, i.e., iron (Fe), cobalt (Co), nickel (Ni), manganese (Mn), and copper (Cu), supported on conductive carbon. The FeCoNiMnCuO HEO powdery catalysts were obtained by ultrafast Joule heating of precursor metal salts on carbon supports, followed by natural oxidation under ambient atmosphere. When used to catalyze SOR in seawater, FeCoNiMnCuO HEO NPs exhibit outstanding performance, requiring a potential of only 0.545 V versus reversible hydrogen electrode (RHE) to attain a current density of 500 mA cm^{-2} and being able to maintain outstanding catalytic stability at 500 mA cm^{-2} over 100 h with minimal degradation. Our comprehensive synchrotron X-ray absorption spectroscopy (XAS) and in situ Raman spectroscopy reveal that the in situ formed metal sulfide layer is the true catalytically active species for SOR. This is also confirmed by our density functional theory (DFT) calculations, which demonstrate that the high-entropy effect helps to reduce the free energy cost of the SOR potential-determining step by increasing the intrinsic charge stability. Furthermore, we fabricate a membrane electrode assembly (MEA) using carbon-supported FeCoNiMnCuO HEO NPs as the anode catalysts for SOR and commercially available Pt/C as the cathode catalysts for HER, and test its performance in a single cell electrolyzer. The electrolyzer can operate continuously for more than 500 h at an industry-relevant current density of 500 mA cm^{-2}, with a cell voltage of just 1.07 V and energy consumption as low as 2.4 kWh m^{-3} H_2. showing great potential for energy-saving, chlorine-free seawater electrolysis for H_2 production.

2. Results and Discussion

2.1. Morphology and Structure of Catalysts

FeCoNiMnCuO HEO catalysts were synthesized through a multistep process involving wet chemical loading of precursor salts on carbon supports and subsequent freeze-drying, followed by ultrafast reduction at a high temperature via Joule heating (**Figure 1a**) and subsequent natural oxidation under ambient conditions. In a typical experiment, a precursor solution containing equimolar metal (Fe, Co, Ni, Mn, and Cu) nitrate salts was mixed with acid-treated carbon black (see Experimental Section) at a target catalyst loading mass (e.g., 50 wt%). After freeze-drying, the resulting powders were wrapped into a piece of flexible carbon paper (50 µm thick), which was then loaded into the chamber of the Joule-heating system. When a large transient current was applied between the two ends of the conductive carbon paper, the temperature rapidly reached ≈1000 °C within just 50 ms, delivering an ultrahigh ramping rate in the order of 10^5 °C s^{-1}. Afterward, the temperature dropped quickly in a few seconds (Figure 1b). The extremely short heating duration (≈50 ms) cannot only effectively reduce metal nitrates to alloy NPs, but also inhibit the overgrowth of NPs and prevent them from agglomeration.[31] Meanwhile, ultrafast cooling allows for kinetic control of the crystallization process and restrains thermodynamic mixing of various components, enabling the formation of high-entropy alloy (HEA) NPs with small sizes.[32] It is worth mentioning that the as-prepared

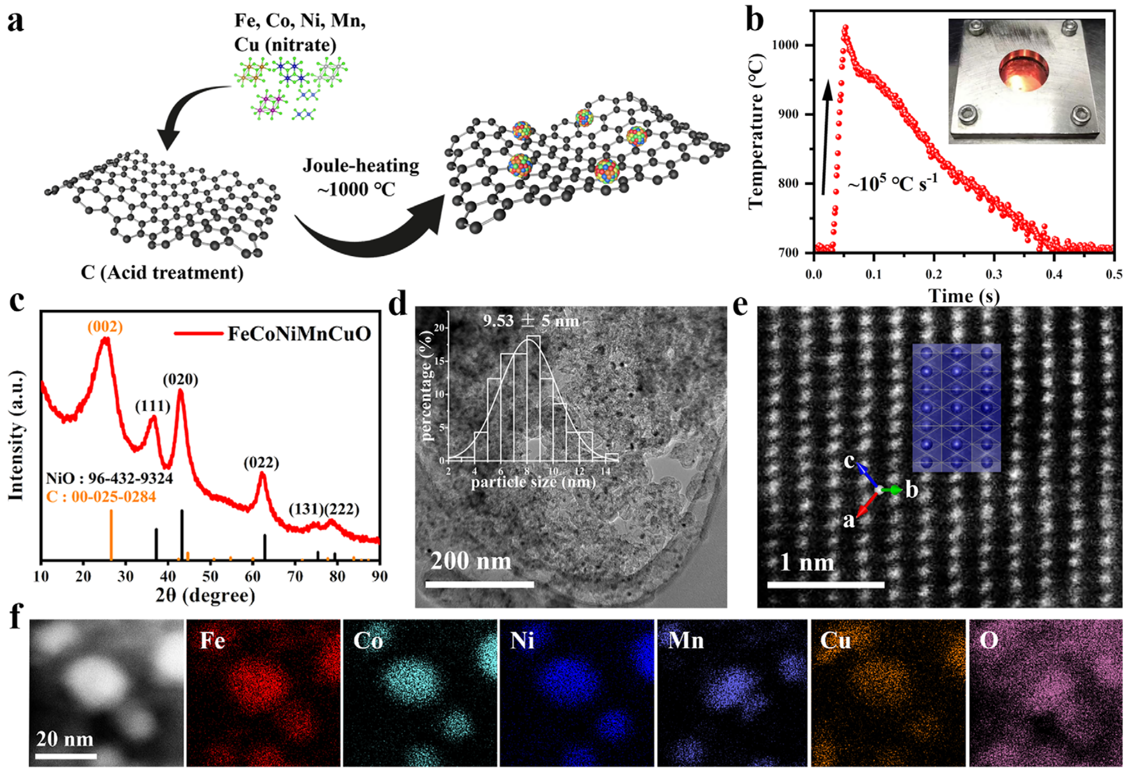

Figure 1. a) Schematic illustration of the synthesis of FeCoNiMnCuO HEO NP catalysts. b) The curve showing the temperature change as a function of time during Joule heating. The detector can only probe temperatures above 700 °C. c) XRD pattern of the FeCoNiMnCuO HEO catalysts. For comparison, the standard diffraction pattern of rock-salt NiO is given. d) image of FeCoNiMnCuO HEO catalysts Inset of (d): a histogram showing the size distribution of FeCoNiMnCuO NPs. e) Cs-corrected STEM image projected perpendicular to the (121) lattice plane. f) HAADF-STEM image and the corresponding elemental maps of FeCoNiMnCuO HEO catalysts.

HEA NPs are metastable in air and can be easily transformed into the corresponding more stable HEO NPs under ambient conditions in a short period of time (from a few to tens of hours).

X-ray diffraction (XRD) examination was carried out to investigate the crystal structure of as-prepared HEA NP catalysts and their transformation upon exposure in air. For comparison, other representative monometallic and bimetallic alloys, including Ni, Co, and CoNi, as well as medium-entropy alloys such as FeCoNi and FeCoNiCu, were also synthesized in a similar way. The freshly prepared HEA was found to show diffractions typical of the face-centered cubic (fcc) crystal structure (Figure S1a, Supporting Information). In addition, diffraction peaks from MnO (COD: 96-154-1154, COD-Crystallography Open Database) were also observed, suggesting that Mn is more readily oxidized compared to other metals. After storing the samples under ambient conditions for one day, we found that all metal and alloy samples, except Ni (COD of Ni: 96-210-2279), were spontaneously transformed into the corresponding oxides (Figure S1b, Supporting Information), due likely to the small NP size. The peak at ≈25° in all XRD patterns originates from the carbon support (Figure S1c, Supporting Information). It's also observed that the crystal phase of all samples did not change notably anymore afterward, indicating that the obtained oxides are stable in air. It is interesting to note that upon exposure under ambient conditions over one day, the diffractions from MnO impurity phases disappeared, and the FeCoNiMnCu HEA was transformed to a single-phase FeCoNiMnCuO (Figure 1c), with peaks located at 37.2°, 43.2°, 62.8°, 75.3°, and 79.3° that can be assigned to the diffractions of (1 1 1), (0 2 0), (0 2 2), (1 3 1), and (2 2 2) crystal planes of the rock-salt structure, similar to that of NiO (COD: 96-432-9324).[33] In contrast, the alloy-to-oxide transformation in CoNi, FeCoNi, and FeCoNiMn was incomplete, as evidenced by the presence of the diffraction peak at 51.8° that can be assigned to the (0 2 0) crystal plane of these fcc alloys. It is believed that high entropy might play a role in such a transformation, which is conducive to the formation of a single-phase HEO. However, detailed phase transformation processes deserve further investigation in the future. Given the naturally oxidized samples are more stable in air and show better electrocatalytic performance for the SOR (Figure S2, Supporting Information), the FeCoNiMnCuO HEO was used in all following studies.

The spatial distribution of FeCoNiMnCuO NPs on carbon and their microstructure were further investigated by transmission electron microscopy (TEM). FeCoNiMnCuO NPs were found to distribute on the carbon support with a high density (Figure 1d), and their sizes vary from 2 to 14 nm with an average of 9.53 ± 5 nm (Figure 1d, inset). Moreover, the densely distributed FeCoNiMnCuO NPs were also clearly resolved under scanning transmission electron microscopy (STEM) observation (Figure S3, Supporting Information). It is noted that the Joule heating temperature and thermal pulse duration play an important role in controlling the sizes of derived NPs. When the

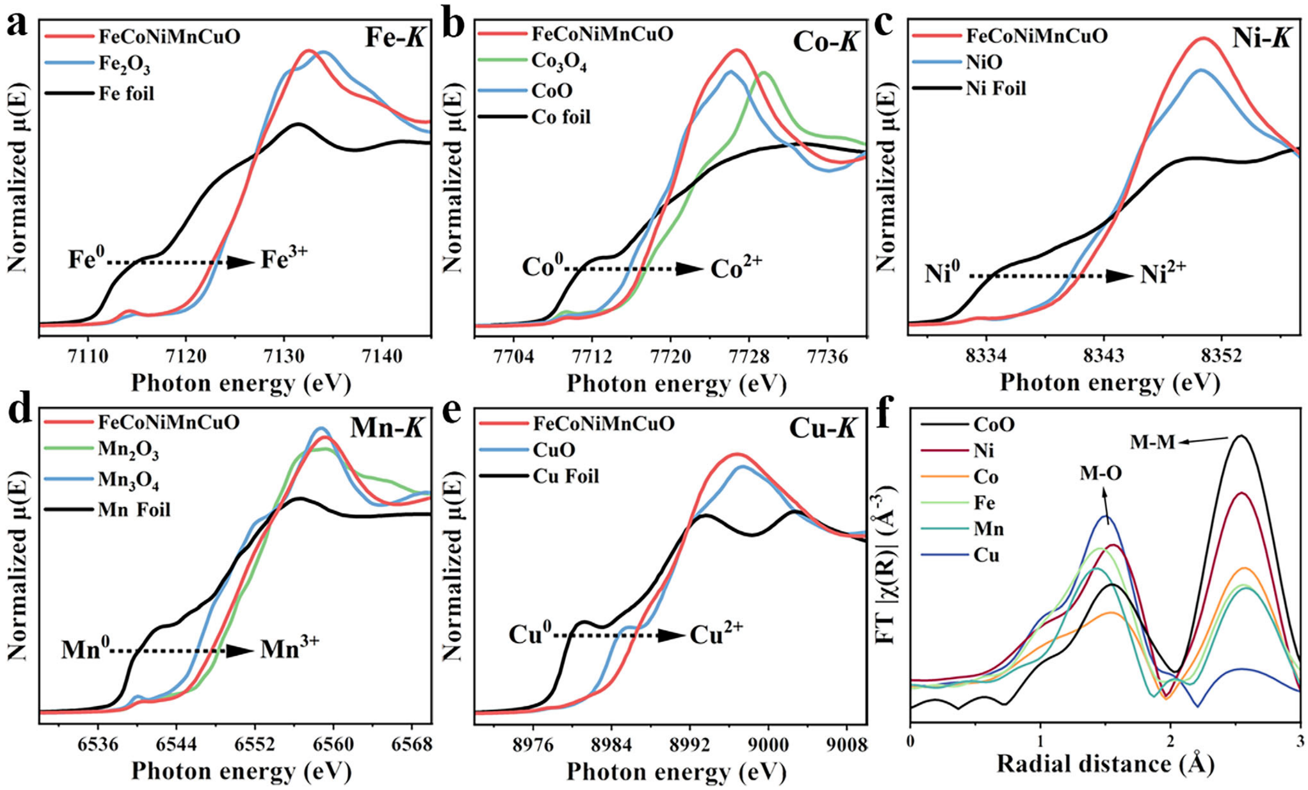

Figure 2. K-edge XANES spectra of a) Fe, b) Co, c) Ni, d) Mn, and e) Cu for the FeCoNiMnCuO HEO NP catalysts, along with the corresponding metal foils and standard oxide samples (Fe_2O_3, CoO, Co_3O_4, NiO, Mn_2O_3, Mn_3O_4, and CuO). f) k^2-weighted FT-EXAFS spectra of FeCoNiMnCuO HEO NP catalysts at the corresponding metal K-edges (FT k range: 3.6–11.4 $Å^{-1}$ for Fe K-edge, 3.4–11.4 $Å^{-1}$ for Co K-edge, 3.3–12 $Å^{-1}$ for Ni K-edge, 3.65–11.2 $Å^{-1}$ for Mn K-edge, and 3.5–12.8 $Å^{-1}$ for Cu K-edge).

Joule heating was performed at ≈800 °C, the obtained NPs were roughly 3 nm in size (Figure S4a,b, Supporting Information). At higher temperatures (e.g., 1300 °C) or with a longer pulse duration (e.g., 5 s) at ≈1000 °C, NPs with much larger sizes appeared and became dominant (Figure S4c–f, Supporting Information). Preliminary SOR tests revealed that the sample prepared at ≈1000 °C with a pulse duration of 50 ms showed notably higher activity than other controls (Figure S5a, Supporting Information). In addition, the "1000 °C_50 ms" sample also exhibited the smallest charge transfer resistance and Tafel slope as well as the largest electrochemically accessible surface area (ECSA, Figures S5b,c and S6, Supporting Information), demonstrating the best electrocatalytic performance, which may result from the small NP size and reasonably good crystallinity. Therefore, the "1000 °C_50 ms" sample was selected for subsequent comprehensive investigations. Aberration (Cs)-corrected scanning transmission electron microscopy (STEM) examination of the FeCoNiMnCuO NPs displayed a clear well-defined atomic arrangement perpendicular to the (121) lattice plane (Figure 1e). Furthermore, the elemental distribution of FeCoNiMnCuO NPs was investigated under the high-angle annular dark-field STEM (HAADF-STEM) mode. All elements are virtually distributed evenly over individual NPs, however, phase separation is also occasionally observed on a nanometer scale in smaller NPs (e.g., bottom left corner, Figure 1f). Semi-quantitative energy-dispersive X-ray spectroscopy (EDS) analysis revealed that the atomic ratio of Fe:Co:Ni:Mn:Cu is ≈2.79:2.92:1.60:1.50:3.24 (Figure S7a, Supporting Information). More precise quantification was done by the inductive-coupled plasma optical emission spectroscopy (ICP-OES) analysis (Figure S7b, Supporting Information), by which the molar ratio of Fe:Co:Ni:Mn:Cu was measured to be 2.97:3.94:4.04:3.92:3.70. Besides, control samples including CoO and FeCoNiO NPs were also characterized by TEM, from which the densely populated NPs and homogeneous distribution of corresponding elements were also confirmed (Figures S8 and S9, Supporting Information).

The oxidation state and local coordination environment of all five metal elements in the FeCoNiMnCuO HEO NPs were systematically studied by synchrotron-based X-ray absorption spectroscopy (XAS) at the corresponding K-edges, along with their standard metallic foils and common oxides. In the X-ray absorption near-edge structure (XANES) region, the FeCoNiMnCuO spectra share similar absorption position (at 0.8 edge jump height) with Fe_2O_3, CoO, NiO, Mn_2O_3, and CuO references at the Fe-K, Co-K, Ni-K, Mn-K, and Cu-K edges, respectively, indicating that the oxidation states of Fe, Co, Ni, Mn, and Cu in FeCoNiMnCuO are +3, +2, +2, +3, and +2, respectively (**Figure** 2a–e). The reason why the absorption edge of HEO is not exactly the same as that of the reference samples is due to the complex local coordination environment and electronic interactions between multiple metal elements in the high-entropy oxide. The chemical states of the surface of FeCoNiMnCuO NPs were also examined by X-ray photoelectron spectroscopy (XPS), and the same oxidation states were found to exist for each metal species (Figure S10a–e, Supporting Information). Further inspection of the XANES region reveals clear deviations in pre-edge features, white-line shape and intensity, and post-edge oscillation, compared to the counterparts of the oxide benchmarks, suggesting the interaction among Fe, Co, Ni, Mn, and Cu on electronic structure and local coordination geometry. To further elucidate the local coordination environment and atomic mixing of the five transition metals in FeCoNiMnCuO NPs, the extended X-ray absorption fine structure (EXAFS) regions were also investigated. The Fourier transforms of EXAFS (FT-EXAFS) are dominated by two features, namely, a metal-oxygen bonding (M−O) at ≈1.5 Å and a metal-metal scattering path (M−M) at ≈2.6 Å (Figure 2f; Figure S11, Supporting Information). EXAFS fitting further quantifies that all five metals share a similar length of the M−M scattering path, 3.018 Å for Fe, 3.014 Å for Co, 2.989 Å for Ni, 3.026 Å for Mn, and 3.007 Å for Cu (Figure S12 and Table S1, Supporting Information). Such a local coordination is similar to that of CoO and NiO references but slightly deviates from that of CuO, Fe_2O_3, and Mn_2O_3. The good similarity suggests all five metals of the FeCoNiMnCuO are well mixed and adopt a rock-salt structure similar to that of CoO and NiO, in agreement with the XRD results. The low intensity of M−M scattering in Cu K-edge EXAFS implies that Cu atoms are primarily located at defect sites and/or on the surface of NPs.

2.2. SOR Performance

The SOR performance of the FeCoNiMnCuO HEO catalyst, along with other control medium-entropy and monometallic/bimetallic oxide samples, was evaluated in natural seawater in the presence of Na_2S using a three-electrode system in an H-type electrolytic cell. Seawater was pre-treated to remove metal cations such as Mg^{2+} and Ca^{2+} (See Experimental Section). A cation exchange membrane (Nafion NR212) was employed to separate the cathodic and anodic compartments and to prevent the crossover of S^{2-} anions and negatively charged polysulfides. The concentration of Na_2S in seawater was optimized at first. The anodic current density increased with the Na_2S concentration up to 2.0 M, and further increase in the concentration to 2.5 M did not lead to a significant change in current density (Figure S13, Supporting Information), suggesting that the mass transport of S^{2-} ions to the reaction front is not the limiting factor in this case. Therefore, 2.0 M Na_2S was adopted as the optimized concentration in the electrolyte. To demonstrate the advantage of SOR over OER, the OER performance of the FeCoNiMnCuO HEO catalysts was also assessed (see Experimental Section). As shown in **Figure 3a**, the FeCoNiMnCuO catalyst can achieve a current density of 100 mA cm^{-2} at an ultralow potential of 0.351 V versus RHE (V_{RHE}) in seawater in the presence of 2.0 M Na_2S. In contrast, it requires a potential as large as 1.701 V_{RHE} to attain the same current density in alkaline seawater (i.e., 1.0 M NaOH + seawater), demonstrating prominent advantages of the SOR over the OER in terms of energy saving (voltage drop as large as 1.35 V at 100 mA cm^{-2}). Figure 3b further compares the SOR and OER performance of the FeCoNiMnCuO HEO catalyst in natural seawater, where it is seen that the potential needed to deliver 300 mA cm^{-2} is as high as 1.813 V_{RHE} for OER, while that for SOR is merely 0.473 V_{RHE}, under which neither the notorious CER nor the carbon support oxidation would be triggered. Figure 3c presents the linear scan voltammetry (LSV) curves of all catalysts under investigation toward the SOR, where it is shown that the SOR performance improves as the number of metal elements in the oxide catalysts increases. The FeCoNiMnCuO NPs show the best SOR activity, requiring only 0.545 V_{RHE} to achieve a high industry-relevant current density of 500 mA cm^{-2}, which outperforms FeCoNiCuO (0.582 V_{RHE}), FeCoNiO (0.662 V_{RHE}), CoNiO (0.705 V_{RHE}), Ni (0.721 V_{RHE}), and CoO (0.752 V_{RHE}) NPs prepared in the same way. Moreover, the SOR activity of different electrocatalysts at various current densities was further compared. As the number of metal elements in the catalyst increases, the anodic potential required to deliver a given current density drastically decreases (Figure 3d), highlighting the advantage of the high-entropy effect in FeCoNiMnCuO HEO NPs.

Tafel analysis was performed to study the SOR reaction kinetics. FeCoNiMnCuO NPs show a lower Tafel slope (62.5 mV dec^{-1}) compared to other controls, indicating much faster charge transfer kinetics (Figure 3e). Additionally, the ECSA of various electrocatalysts was estimated by assessing their electrochemical double-layer capacitance (C_{dl}, Figure S14, Supporting Information). The FeCoNiMnCuO electrocatalyst exhibits a larger ECSA (Figure S15a, Supporting Information), implying that there are likely more active sites exposed that can contribute to the SOR. Furthermore, electrochemical impedance spectroscopy (EIS) was employed to analyze interfacial charge transfer processes. The results show that FeCoNiMnCuO NPs possess the lowest charge transfer resistance (R_{ct}) among all catalysts under investigation, which suggests efficient electron transport at the catalyst-electrolyte interface and consequently the accelerated SOR kinetics (Figure 3f). Besides, we also evaluated the SOR kinetics over a wider current density range by plotting the overpotential change ($\Delta\eta$) as a function of the variation of logarithm of current densities ($\Delta log\,|j|$).[34] Usually, the lower the value of $\Delta\eta$ / $\Delta log\,|j|$, namely $R_{\eta/j}$, the better the charge and mass transfer during the electrochemical reaction. As shown in Figure S15b (Supporting Information), at low current densities, all electrocatalysts show similar $R_{\eta/j}$ values. However, at high current densities, the FeCoNiMnCuO NPs reveal notably lower $_{R\eta/j}$ than all others, demonstrating outstanding reaction kinetics.

As a key figure of merit, the electrocatalytic stability of FeCoNiMnCuO HEO NPs toward SOR was further assessed in a three-electrode cell using chronopotentiometry (CP), in which the seawater electrolyte was continuously replenished by a peristaltic pump. Remarkably, at an industry-relevant current density of 500 mA cm^{-2}, the catalyst could stably catalyze the SOR at ≈0.6 V_{RHE} with nearly no degradation for 100 h (Figure 3g), demonstrating outstanding long-term stability. The fluctuations in the CP curve originate from the consumption and replenishment of Na_2S in the electrolyte. It is worth noting that at this anodic potential the oxidation of carbon supports does not take place,[35] which also to a certain extent contributes to the superior long-term stability of FeCoNiMnCuO NPs toward SOR in seawater.

The SOR products at industry-relevant current density were further analyzed by UV–vis spectroscopy. To do so, the electrolyte was sampled at regular intervals when various NP catalysts were used to catalyze the SOR at 500 mA cm^{-2}. It was observed that as the reaction progressed, the color of the electrolyte

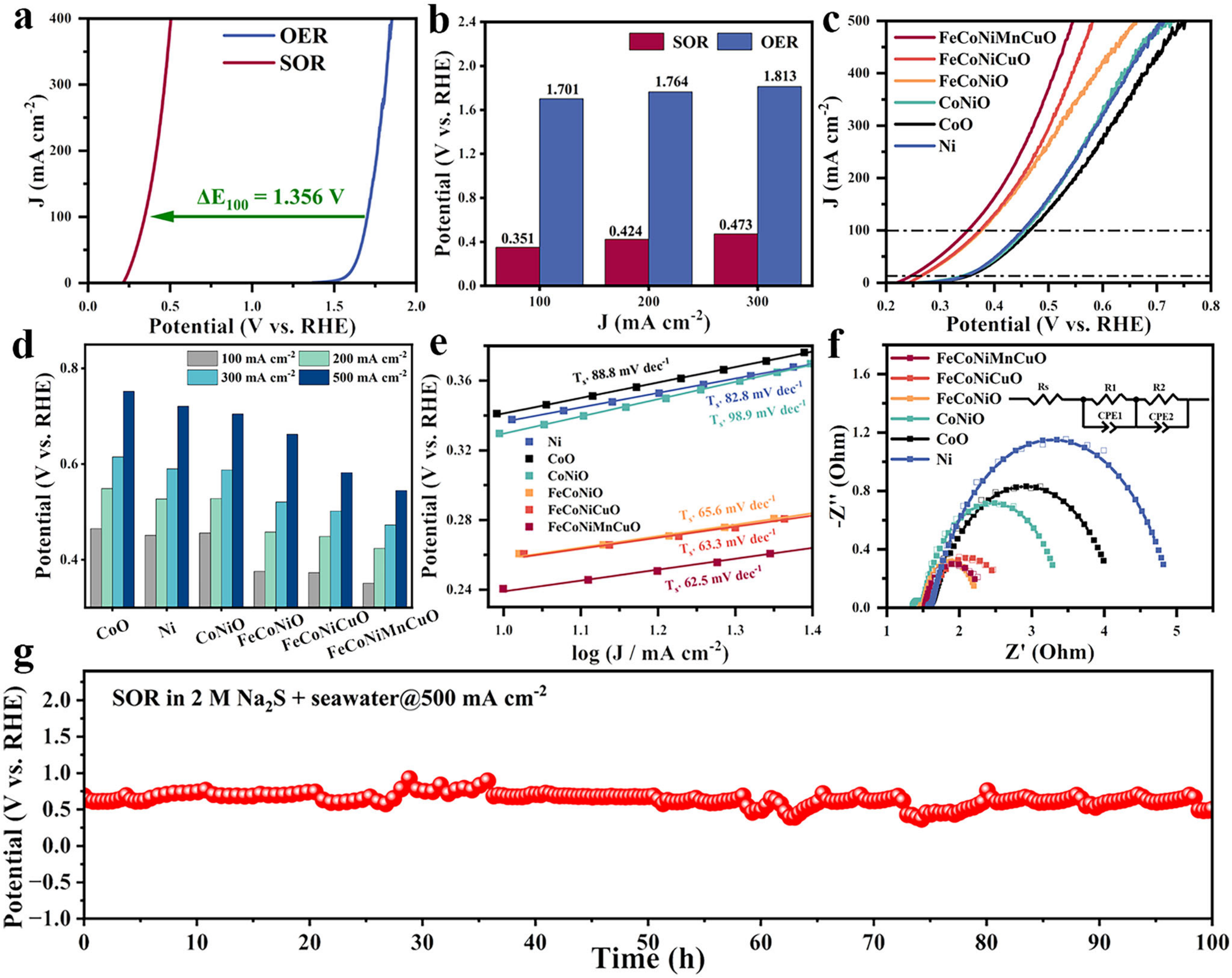

Figure 3. Electrocatalytic SOR performance of FeCoNiMnCuO HEO and other control catalysts. a) LSV curves of the FeCoNiMnCuO HEO NPs for the SOR and OER in alkaline seawater. b) Comparison of overpotentials needed to reach 100, 200, and 300 mA cm^{-2} for the FeCoNiMnCuO HEO NP catalysts during the SOR and OER. c) Polarization curves of different catalysts acquired during the SOR in 2.0 M Na_2S + seawater (horizontal lines are drawn at 10 and 100 mA cm^{-2} for better visual comparison of activity). d) Comparison of the potentials needed at different current densities for the FeCoNiMnCuO HEO NP catalysts toward the SOR. e) Tafel plots of different catalysts during the SOR. f) Nyquist plots of the FeCoNiMnCuO HEO NP catalysts measured at 0.44 V_{RHE} toward the SOR. Inset: the equivalent circuit model used for plot fitting. g) Long-term catalytic stability of FeCoNiMnCuO HEO NP catalysts assessed at 500 mA cm^{-2} toward the SOR.

gradually changed from colorless to brown, which arises from the increased concentration of short-chain polysulfide intermediates (S_x^{2-}, $2 \leq x \leq 4$) in the electrolyte. Accordingly, in the UV–vis spectra, two absorption bands of the short-chain polysulfide intermediates appear at 300 and 370 nm, and their intensities become stronger and stronger with the increasing SOR time for all NP catalysts under investigation (i.e., CoO, FeCoNiO, and FeCoNiMnCuO). Furthermore, the intensity of the short-chain polysulfide absorption bands rises faster with a more uniform step for FeCoNiMnCuO NPs, compared to that of CoO and FeCoNiO NPs (Figure S16a–c, Supporting Information), confirming that FeCoNiMnCuO HEO NPs have a stronger capability of converting S^{2-} ions to short-chain polysulfide intermediates, in line with their higher SOR catalytic activity. In addition, the anodic electrolyte was collected and acidified by excess hydrochloric acid, and the resulting yellowish solid precipitates were confirmed to be elemental sulfur (S_8, COD: 96-901-1363) by XRD (Figure S16d, Supporting Information).

To elucidate the origin of the superior SOR activity on FeCoNiMnCuO HEO NPs and to understand the role of each metal, *operando* XAS measurements at the corresponding K-edges were conducted to monitor the possible in situ transformation of FeCoNiMnCuO HEO due to the strong affinity of sulfions/polysulfides to transition metals. To do so, *operando* XAS spectra were collected in a customized spectroelectrochemical cell under three different conditions: 1) with a constant flow of 1.0 м NaOH solution at open circuit potential (OCP_{NaOH}: 0.84 V_{RHE}); 2) with a constant flow of 1.0 м NaOH and 0.1 м Na_2S at OCP_S (0.05 V_{RHE}, data denoted as "w S^{2-}"); 3) with the electrolyte of 1.0 м NaOH + 0.1 м Na_2S at a given SOR potential of 0.55 V_{RHE} (data denoted as "SOR"). Considering possible transition of OCP in the second case, which likely arises from the strong reducing power of S^{2-} anions themselves, additional *operando* XAS measurements were carried out in 1 M NaOH at 0.05 V_{RHE} (data labeled as "w/o S^{2-}") to check the reduction effect of S^{2-} by applying the same potential and to disentangle the interplay of the reduction and sulfidation effects of S^{2-}-containing electrolyte on the surface of HEO electrocatalysts. Indeed, all five metals underwent various extents of reduction, especially Cu to its metallic form, as evidenced by XANES and EXAFS spectra (Figures S17–S19, Supporting Information). Without the interference of the reduction effect, the sulfidation of the HEO is then allowed to be fingerprinted by XANES, exhibiting both valence state and local coordination (**Figure** 4a–e). By comparing the "w S^{2-}" data with the "w/o S^{2-}" data of the corresponding metal sulfides in terms of the line shape of the absorption edge and the white-line intensity, the Cu in HEO NPs is mainly transformed to Cu_2S at OCP, the Ni, Co and Fe largely remain the original oxide forms with only a small fraction of NiS, CoS_2 and FeS_2 generated, respectively, and the Mn remains unaltered in the presence of S^{2-}. Such a reactivity trend is consistent with the hard-soft-acid-base (HSAB) theory, according to which Cu has the strongest affinity with S and Mn has the weakest affinity among the five transition metals studied. During the SOR, the Cu in HEO NPs is further transformed from Cu_2S into CuS, as indicated by the peak at ≈8986 eV; the Co and Ni increase their fraction of corresponding sulfides; the Fe slightly increases in the oxidation state, as evidenced by the edge shift toward the higher energy, and the Mn remains stable. The formation of metal sulfides in the above cases was confirmed by FT-EXAFS spectra (Figure 4f–j) and WT-EXAFS (Figure S20, Supporting Information), which can be seen from the increased contribution of metal-sulfur scattering in the first-shell coordination. During the acquisition of the "SOR data", an anodic potential (0.55 V_{RHE}) was applied to enable SOR to happen. Therefore, compared to the "w S^{2-} data" measured at OCP (i.e., 0.05 V_{RHE}), the valence state of active metal species is expected to increase and the resulting metal-sulfur bonding is accordingly anticipated to be strengthened, drawing electrons from the surface-adsorbed S^{2-}. Both cases are found for Cu and Fe in HEO NPs. From the above XAS analysis, we believe that the true catalytically active species for SOR are metal sulfides formed spontaneously when FeCoNiMnCuO NPs are in contact with S^{2-} anions, and Cu and Fe are largely involved in the SOR process, consistent with the aforementioned electrochemical results where the addition of Cu and Fe promotes SOR activity to a greater extent than other elements. The findings also align with recent studies about the SOR catalysts.[28] While the *operando* characterization primarily captured signals of Fe–S and Cu–S species due to the resolution and sensitivity limitations of the *operando* technique per se, it is likely that other elements also contribute to the reaction. For example, Mn could act as an electron acceptor to stabilize the Fe/S interface or participate in polysulfide intermediate formation, and Ni and Co might also form trace sulfides, helping stabilize the HEO NPs.

The in situ transformation of FeCoNiMnCuO NPs in the presence of S^{2-} at OCP and during SOR was further studied by quasi-in situ XAS at the S K-edge (Figure 4k). At the OCP, the XAS spectrum shows a strong peak at ≈2470.6 eV corresponding to transition metal sulfide, with a polysulfide shoulder at 2472 eV, which confirms the spontaneous chemical reaction between FeCoNiMnCuO and S^{2-}, yielding metal sulfide and adsorbed polysulfide species. After the SOR, a low-energy shoulder at ≈2468.8 eV appears, and the contribution of the polysulfide shoulder decreases significantly. As the transition metal sulfide peak describes the electron transition from S 1s to S 3p hybridized with the unoccupied 3d e_g orbital of transition metals, the low-energy shoulder suggests the increased covalence between transition metals and sulfur after the SOR, in line with the increased oxidation state of transition metals (Fe and Cu) during SOR (Figure 4a–e). Furthermore, post-SOR XPS analysis revealed that signals arising from S appear at 161.81 and 167.83 eV for FeCoNiCuMnO HEO NPs after the SOR (Figure 4l), which can be attributed to the metal sulfide and metal sulfate, respectively.[30,36]

To further elucidate the accelerated SOR process on the FeCoNiMnCuO HEO NPs, in situ Raman spectroscopy study was carried out. No obvious Raman signals were found in the range of 250–800 cm^{-1} for the electrolyte (2.0 M Na_2S + seawater) and at the OCP (Figures S21–S23, Supporting Information). As the applied anodic potential increases, two Raman bands begin to appear at 450 and 475 cm^{-1}, which can be attributed to the symmetric stretching vibrations of short-chain polysulfides. Specifically, the peak at ≈450 cm^{-1} likely corresponds to $S_3{}^{2-}$ or $S_4{}^{2-}$,[37] and the peak at ≈475 cm^{-1} is associated with $S_2{}^{2-}$,[38] agreeing well with the UV–vis data. However, the dynamic change of these two Raman bands differs from one sample to the other. When compared with CoO and FeCoNiO NPs, the characteristic Raman peaks appear in FeCoNiMnCuO HEO at a much earlier potential of 0.4 V_{RHE}; moreover, at the same potential, the band intensities for FeCoNiMnCuO HEO are much stronger than those of CoO and FeCoNiO samples (Figure 4m–o; Figure S21–S23, Supporting Information), which confirms the lower overpotential and faster reaction kinetics delivered by FeCoNiMnCuO HEO NPs toward the SOR.

The spin-polarized DFT calculations were performed to investigate the origins of SOR activity and the impact of the high-entropy effect on the SOR performance. As discussed above (Figure 1c), the FeCoNiMnCuO HEO NPs exhibit a crystal structure similar to NiO with (020) planes being dominant. Therefore, the (020) plane of rock-salt structure metal oxides was adopted to construct models for calculations (Figure S24, Supporting Information). According to the previous DFT calculations,[25,27,28] various sulfur species show a strong tendency to adsorb on the transition metal sites exposed on the surface of electrocatalysts. We also calculated the adsorption energy of sulfur on the metal oxide surface. The results reveal that all oxide surfaces have strong sulfur affinity with the single sulfur atom adsorption energy as low as −2.5 eV, indicating the enrichment of sulfur over the oxide surface. Therefore, following the procedures reported in the literature,[28,39] the models were constructed by covering the sulfur-philic oxide surfaces with a monolayer of sulfur (denoted as CoO@S, NiO@S, FeO@S, FeCoNiO@S, and FeCoNiMnCuO@S) to implement subsequent SOR calculations (Figure S25, Supporting Information). The formation energies of the sulfur layer are −0.16, −0.08, −0.62, −0.27, and −0.30 eV per sulfur atom for CoO, NiO, FeO, FeCoNiO, and FeCoNiMnCuO, respectively, where the negative values indicate the easy formation of the sulfur layer on catalyst surfaces. **Figure** 5a shows the free energy profiles of all elementary steps taking place on

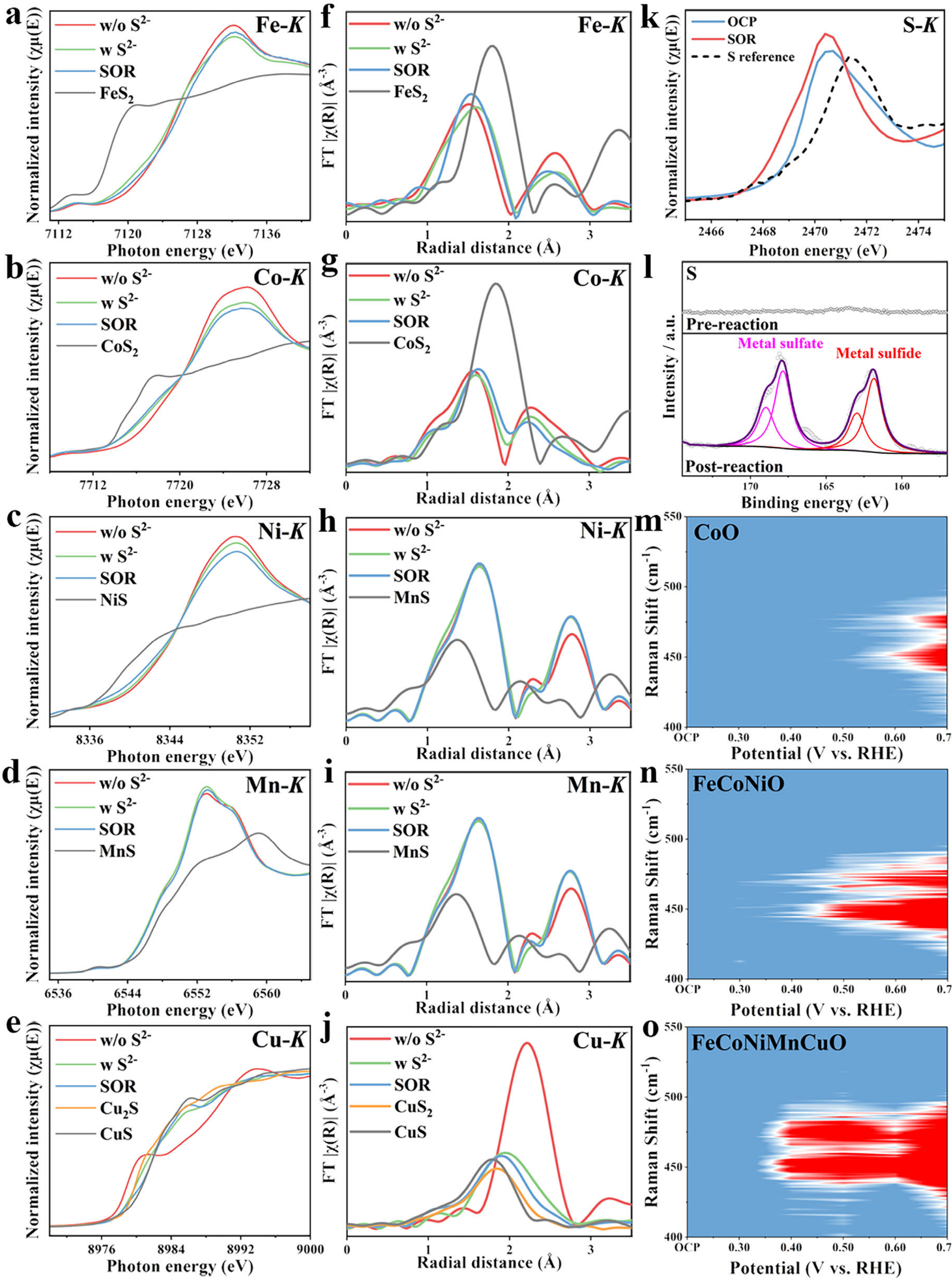

Figure 4. a–e) *operando* metal K-edge XANES spectra and f–j) *operando* k^2-weighted FT-EXAFS spectra of different transition metals in the FeCoNiMnCuO HEO NPs, acquired at the OCP in alkaline solutions (1.0 м NaOH) with and without S^{2-}, as well as during the SOR (FT k range: 2.5–10 Å^{-1} for Fe K-edge, 3.5–11 Å^{-1} for Co K-edge, 2.4–10 Å^{-1} for Ni K-edge, 2.3–9.3 Å^{-1} for Mn K-edge, and 2.8–10.7 Å^{-1} for Cu K-edge). k) Quasi-in situ XANES spectra of S K-edge for the catalyst acquired at the OCP$_S$ and after SOR. l) High-resolution S 1s XPS spectra before and after the SOR. 2D in situ Raman spectral maps collected on m) CoO, n) FeCoNiO, and o) FeCoNiMnCuO NP catalysts. Electrolyte: 2 м Na$_2$S + seawater.

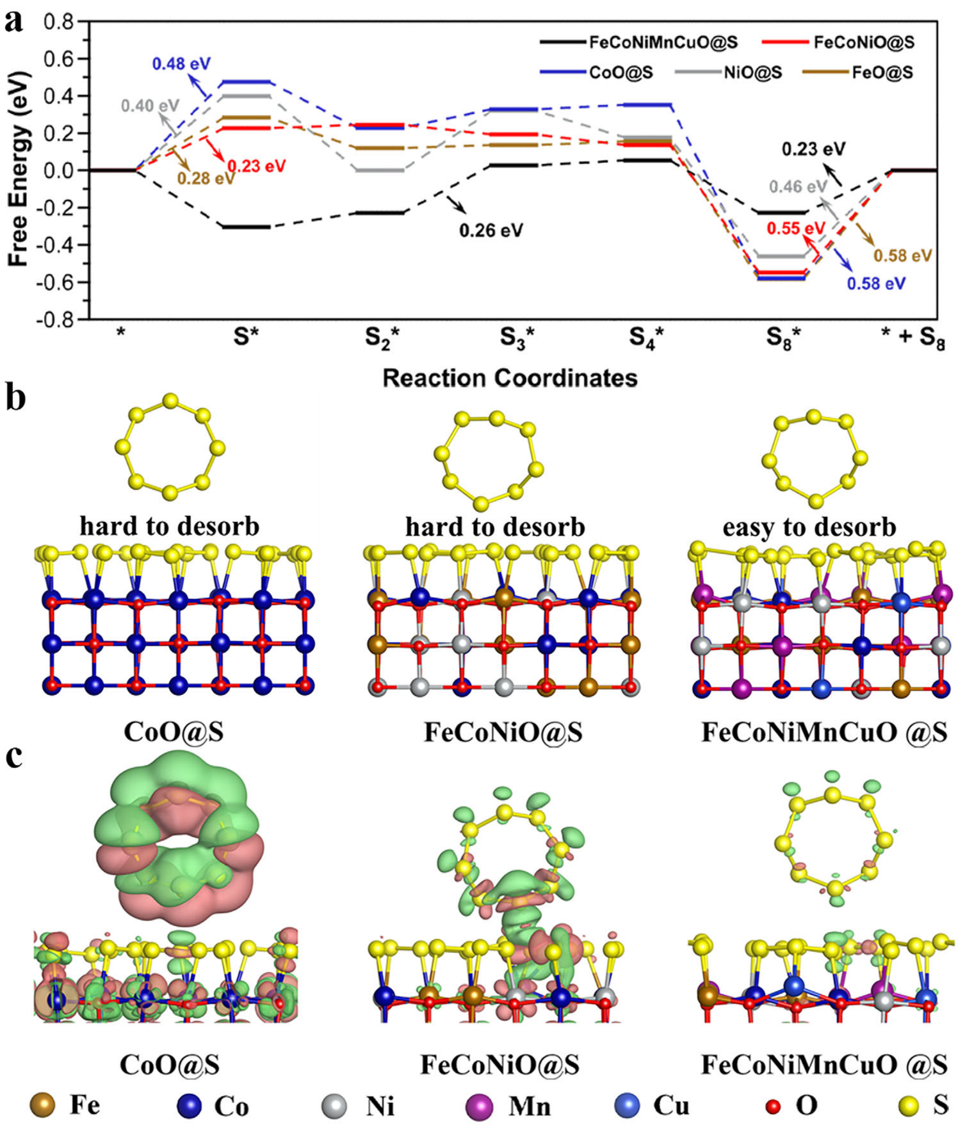

Figure 5. The spin-polarized DFT calculations. a) The free energy profiles of the SOR process on different electrocatalysts, calculated under the theoretical equilibrium potential of 0.14 V_{RHE}. b) The 3D configurations of S_8 over the different catalysts for desorption. c) The charge density diagram showing the electron exchange between the S_8 and CoO@S, FeCoNiO@S, and FeCoNiMnCuO@S catalysts during the S_8 desorption. Electron depletion and accumulation are depicted by pink and green areas, respectively. The isosurfaces are plotted at the value of ± 0.01 |e| Å^{-3}.

different model catalysts. The 3D configurations of different sulfur species sitting on FeCoNiMnCuO@S are presented in Figure S26 (Supporting Information). The adsorption of S^{2-} on FeCoNiMnCuO@S is spontaneous in thermodynamics, while that on CoO@S, NiO@S, FeO@S, and FeCoNiO@S is an uphill, endergonic process. The potential-determining step (PDS) for all catalysts is the hard desorption of S_8 product. For this step, the CoO@S, NiO@S, FeO@S, and FeCoNiO@S surfaces suffer from relatively high desorption free energies varying from 0.46 to 0.58 eV (Figure 5b; Table S3, Supporting Information), while the desorption free energy for FeCoNiMnCuO@S is markedly lower (0.23 eV), indicating that the high entropy in HEO indeed promotes the SOR activity, in good agreement with our experimental results (Figure 3). Further charge distribution analysis shows that during the S_8 desorption, the FeCoNiMnCuO@S exhibits higher charge stability (Figure 5c), compared to CoO@S and FeCoNiO@S. Moreover, the Bader charge changes of the surface sulfur layer (Δq) during the S_8 desorption also play the same role. The absolute value of Δq on the FeCoNiMnCuO@S surface is the lowest (0.08 |e|, Figure S27, Supporting Information), much smaller than that on FeCoNiO@S (0.11 |e|) and CoO@S (0.15 |e|), suggesting that the disturbance on the HEO surface is insignificant. Our DFT calculations demonstrate that the high-entropy effect of the FeCoNiMnCuO NPs lowers the free energy cost of the SOR potential-determining step and meanwhile, increases the internal charge stability, making FeCoNiMnCuO the most active catalyst for SOR, which rationally explains our experimental observations.

The overall seawater electrolysis performance was further evaluated in pre-treated natural seawater in the presence of

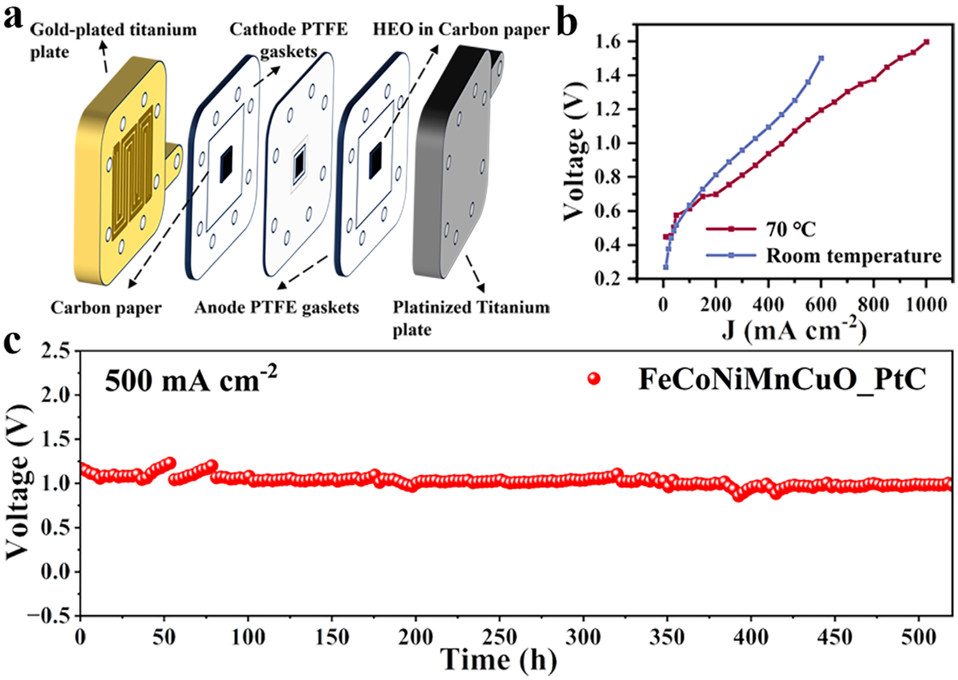

Figure 6. a) Schematic illustration of the asymmetric seawater electrolyzer. b) Polarization curves recorded at room temperature and 70 °C. c) Long-term operational stability of the electrolyzer assessed at 500 mA cm^{-2} at 70 °C.

2.0 M Na_2S, using the FeCoNiMnCuO HEO NPs as the anode catalysts and commercially available Pt/C as the cathode catalysts (**Figure** 6a, see Experimental Section). The electrolyzer requires 1.2 V to deliver 500 mA cm^{-2} at room temperature (Figure 6b). When the temperature is increased to 70 °C, the voltage needed to afford 500 mA cm^{-2} is markedly lowered to just 1.07 V, which can be translated to the energy consumption of merely 2.4 kWh per m^3 of H_2, significantly smaller than that of conventional seawater electrolysis (>4.5–6.0 kWh m^{-3} H_2).[40] More importantly, the SOR-assisted seawater electrolysis system demonstrated excellent long-term stability at 70 °C, able to continuously operate at 500 mA cm^{-2} for more than 500 h without degradation (Figure 6c), representing a remarkable advance in operating current density and durability compared to previously reported SOR-assisted hybrid water electrolysis (Table S2, Supporting Information). The fluctuations in the CP curve originate from the consumption and replenishment of Na_2S in the electrolyte.

3. Conclusion

In conclusion, we successfully synthesized FeCoNiMnCuO high-entropy oxide nanoparticulate catalysts supported on carbon black, taking advantage of the ultrafast Joule-heating method, which demonstrates exceptional SOR performance in alkaline natural seawater, particularly at high current densities. We performed comprehensive in situ XAS and Raman spectroscopy studies and proved that the true catalytically active species are the metal sulfide layer formed on the surface of FeCoNiMnCuO NPs in the presence of S^{2-} anions. Furthermore, our DFT calculations show that the free energy cost of the potential-determining step on high-entropy FeCoNiMnCuO is much lower than that on other medium-entropy and monometallic oxide catalysts, highlighting the favorable high-entropy effect on the SOR performance. Finally, we demonstrated SOR-assisted seawater electrolysis in a single-cell electrolyzer, which can stably operate at an industry-relevant current density of 500 mA cm^{-2} over 500 h without notable performance decay. Replacing the energy-demanding OER with SOR driven by the high-performance FeCoNiMnCuO HEO catalysts enables more than 50% reduction in energy consumption for SWE. Besides, the ultra-short thermal pulses (50 ms) applied during the Joule-heating also substantially reduce the energy consumption during materials synthesis. From the cost perspective, raw materials of transition metals used in this work are nearly three-orders of magnitude cheaper than those of iridium-based materials that are typically used in seawater electrolysis for their good corrosion resistance. Hence, the powdery transition metal HEO NP catalysts reported in this work hold significant potential for low-cost, energy-saving and chlorine-free hydrogen production from seawater.

4. Experimental Section

Materials Preparation: To make the carbon support surface hydrophilic, 2 g carbon black (CB, AkzoNobel) was dispersed into a mixed solution containing 85 mL deionized (DI) water, 15 mL nitric acid (HNO_3), and 50 mL hydrogen peroxide (H_2O_2). The mixture was then heated to 85 °C in an oil bath under constant magnetic stirring for 10 h. Subsequently, the obtained solution was diafiltrated and thoroughly washed with DI water and ethanol several times. Afterward, the collected product was freeze-dried and then used as supporting materials to load HEO NPs. To prepare the precursor solution, equimolar metal salts, including $Fe(NO_3)_3{\cdot}9H_2O$, $Co(NO_3)_2{\cdot}6H_2O$, $Ni(NO_3)_2{\cdot}6H_2O$, $Mn(NO_3)_2{\cdot}4H_2O$ and $Cu(NO_3)_2{\cdot}3H_2O$, were dissolved in DI water under vigorous magnetic stirring. Next, a certain amount of acid-treated CB was dispersed in the precursor solution, and the solution was then stirred for 1 h and ultrasonicated for another 1 h. Subsequently, the resulting mixture was freeze-dried.

Thus-obtained powders were evenly spread on a piece of flexible carbon paper (CP), which was then wrapped up and loaded in the chamber of the flash Joule-heating apparatus (Hefei In situ High-tech Co., Ltd.) in an argon atmosphere. The programmed thermal pulses (input current ~200 A, 50 ms duration) were then applied, leading to a temperature maximum up to 1000 °C, as measured by a high-precision infrared detector (Model lec825, Hefei In situ High-tech Co., Ltd.).

Materials Characterization: Powder X-ray diffraction (XRD) examinations were conducted on an Aeris instrument (Malvern Panalytical) operating at 40 kV and 15 mA with Cu K_{α} radiation ($\lambda = 1.541875$ Å). The 2θ angle was scanned from 10° to 90°with a speed of $0.04^{\circ}s^{-1}$. Transmission electron microscopy (TEM) investigation was carried out on a microscope operating at 200 kV (JEOL JEM-F200). The actual metal contents of HEO-based catalysts were determined by the inductively coupled plasma–optical emission spectroscopy (ICP-OES, Thermo Scientific ™ iCAP ™ 7200). X-ray photoelectron spectroscopy (XPS) characterization was performed on a Thermo Scientific K-Alpha instrument. All XPS spectra were calibrated with respect to the binding energy of C 1s (284.8 eV). In situ Raman spectroscopy examination was done on a confocal Raman spectrometer (Horiba LabRam HR Evolution). Besides, the optical absorption tests of the electrolyte during the reaction were conducted on a UV–vis/NIR spectrophotometer (Hitachi High-Tech UH4150). Metal K-edge X-ray absorption spectra (XAS) were acquired at the B18 beamline of Diamond Light Source (UK) using a Quick EXAFS mode with a ring energy of 3.0 GeV and a ring current of ≈300 mA. For ex situ XAS measurements, each sample was finely ground and mixed with cellulose to form a homogeneous mixture, and then compressed into a pellet. The XAS spectra were measured at Fe-K, Co-K, Ni-K, Mn-K, and Cu-K edges in transmission using ionization chambers, along with the corresponding metal foil in the reference channel for energy calibration. Quasi-in situ S K-edge XAS measurements were carried out at the BL16U1 beamline of the Shanghai Synchrotron Radiation Facility (SSRF, China) with a ring energy of 3.5 GeV and a ring current of ≈210 mA. The S K-edge was measured using a photodiode in fluorescence mode. The measured spectra were processed and analyzed using ATHENA in the Demeter software package.[41]

Electrochemical Measurements: To prepare the catalyst ink, 5 mg of catalysts were homogeneously dispersed into a solution containing 490 µL isopropanol, 490 µL DI water, and 20 µL Nafion solution (5 wt%, Thermo Scientific) by ultrasonication. Afterward, 200 µL the suspension was drop-cast onto a piece of CP (1 cm × 1 cm; catalyst loading: ≈1 mg cm^{-2}). The electrocatalytic OER performance of the FeCoNiMnCuO HEO NPs was evaluated in a three-electrode system at room temperature, using an electrochemical workstation (Bio-logic SAS, VMP-3e). The SOR performance was assessed in an H-cell with a proton exchange membrane (Nafion NR212) to separate the two compartments. The catalyst-loaded CP was employed as the working electrode, and a platinum plate and a Hg/HgO (1 M KOH) electrode as the counter and reference electrodes, respectively. All potentials in this work are converted to the RHE scale according to the following equation:[42]

$$E_{RHE} = E_{Hg/HgO} + 0.0592 \times pH + 0.096 \tag{1}$$

The OER performance of catalysts was appraised in alkaline seawater (i.e., 1.0 M NaOH + seawater, pH ≈ 14.0). For SOR tests, the electrolyte consisting of 2.0 M Na_2S dissolved in seawater was used (pH 13.4). The natural seawater was collected from the Bohai Sea (120.79 °E, 40.59 °N, Jan. 2024). After adding NaOH or $Na_2S{\cdot}9H_2O$ into natural seawater, solid precipitates immediately appeared, which mainly constitute metal hydroxides and salts. The clear solution was then filtered, centrifuged and then employed as the electrolyte in electrocatalytic tests. The apparent OER and SOR activities were assessed using cyclic voltammetry (CV) at a scan rate of 5 mV s^{-1}. 85% iR-correction was applied to compensate the voltage drop between the reference and working electrodes. Electrochemical impedance spectroscopy (EIS) measurements were conducted within the frequency range of 10^5–0.01 Hz with a 10 mV sinusoidal perturbation, and the Nyquist plots were fitted and processed by the Z-View software. The stability of SOR was evaluated through chronopotentiometry (CP) at a constant current density of 500 mA cm^{-2}. The electrochemically accessible surface area (ECSA) was determined through the electrochemical double-layer capacitance (C_{dl}) of catalysts (see below Equation 2), which was estimated by conducting CV in the non-Faradaic potential region of 1.01–1.11 V versus RHE at various scan rates (ν) from 5 to 120 mV s^{-1}, followed by extracting the slope from the resultant $|j_a - j_c|$ / 2 versus ν plots, assuming the specific capacitance value (C_s) to be 0.035 mF cm^{-2}.[42]

$$ECSA = C_{dl}/C_s \tag{2}$$

The FeCoNiMnCuO HEO electrodes for the *operando* XAS measurements were prepared with special care, so as to balance the needs of electrochemistry and spectroscopy and to avoid structural changes of the FeCoNiMnCuO HEO NPs. Specifically, the catalyst ink (5 mg mL^{-1} in H_2O) was applied on one side of the carbon paper (TGPH060, Toray, with a microporous carbon layer), and then dried under an IR lamp. The catalyst loading was calculated by subtracting the mass of the electrode without the catalyst layer from that with the layer, which is ≈1.1 mg cm^{-2}, unless specified otherwise. XAS spectra as a function of applied potentials were collected using a customized spectroelectrochemical cell. A flattened Au wire was used to build up electrical contact with the catalyst electrode, and a Pt coil as the counter electrode, and a Hg/HgO (1.0 M KOH) electrode as the reference electrode. The XAS spectra of different transition metals were measured under potential control. In order to better study the changes in metal valence states, the electrode was tested in two different electrolytes (1.0 M NaOH and 1.0 M NaOH + 0.1 M Na_2S).

In order to validate the performance of catalysts for real-world applications, a membrane electrode assembly (MEA) was constructed. The anode was made by drop-casting the catalyst ink on a piece of CP (active area: 1 cm × 1 cm; catalyst loading: ≈1 mg cm^{-2}), followed by drying under an IR lamp. Commercial Pt/C (TKK) was used as the cathode catalyst for H_2 production. To prepare the ink, ≈100 mg Pt/C were dispersed in a mixed solution containing isopropanol and water (1: 3, v/v), followed by the addition of Nafion solution (Pt/C: Nafion = 2.5:1, m/m), which was then ultrasonicated for 1–2 h. Subsequently, the prepared ink was electro-sprayed onto a PDFE membrane (area: ≈3 cm^2) with a catalyst mass loading of 1 mg cm^{-2}. After that, 1cm^2 of the Pt/C catalyst layer was removed and transferred onto a proton exchange membrane (Nafion NR212) for use as the cathode. In the end, the MEA was assembled by putting the CP-supported FeCoNiMnCuO HEO anode and Pt/C-coated Nafion together, which were then sandwiched by two pieces of carbon paper as the porous gas diffusion layers (GDLs). During the tests, preheated electrolyte consisting of natural seawater and 2.0 M Na_2S was fed to the anodic and cathodic compartments through two separate peristaltic pumps with the same flow rate of 200 mL min^{-1}. The cell temperature was maintained at 70 °C. The stability of the MEA was evaluated by chronopotentiometry at 500 mA cm^{-2}.

Supporting Information

Supporting Information is available from the Wiley Online Library or from the author.

Acknowledgements

W.S., T.-J.H., and H.H. contributed equally to this work. This work is financially supported by the National Key R&D Program (Grant No. 2024YFE0114900) and the Overseas Talent Recruitment Program (Grant No. 22J4021Z311) of the Ministry of Science and Technology of China, as well as by Guangdong Basic and Applied Basic Research Foundation (Grant No. 2024A1515240010) and the start-up grant of the Songshan Lake Materials Laboratory (Grant No. Y2D1051Z311). The authors thank Diamond Light Source for instrument access on B18 (Proposal No. SP36104) and the beamline scientist Veronica Celorrio for her assistance. Additionally, the authors also thank the Shanghai Synchrotron Radiation Facility of BL16U1 (https://cstr.cn/31124.02.SSRF.BL16U1) for the assistance on tender XAS measurements. The computational resources are supported by Songshan Lake HPC Center (SSL-HPC) at Great Bay University and Dongguan Key Laboratory of Artificial Intelligence Design for Advanced Materials (LAIDAM).

Conflict of Interest

The authors declare no conflict of interest.

Data Availability Statement

The data that support the findings of this study are available in the supplementary material of this article.

Keywords

high entropy oxides, joule-heating, operando X-ray absorption spectroscopy, seawater electrolysis, sulfion oxidation reaction

Received: March 11, 2025
Revised: April 27, 2025
Published online:

---

[1] M. S. Dresselhaus, I. L. Thomas, *Nature* **2001**, *414*, 332;
[2] J. A. Turner, *Science* **2004**, *305*, 972.
[3] M. F. Milazzo, F. Spina, P. Primerano, J. C. J. Bart, *Renewable Sustainable Energy Rev.* **2013**, *26*, 579.
[4] M. Balat, M. Balat, *Int. J. Hydrogen Energy* **2009**, *34*, 3589.
[5] D. Mori, K. Hirose, *Int. J. Hydrogen Energy* **2009**, *34*, 4569.
[6] B. Parkinson, P. Balcombe, J. F. Speirs, A. D. Hawkes, K. Hellgardt, *Energy Environ. Sci.* **2019**, *12*, 19.
[7] Z. Yu, C. Si, A. P. LaGrow, Z. Tai, W. A. Caliebe, A. Tayal, M. J. Sampaio, J. P. S. Sousa, I. Amorim, A. Araujo, L. Meng, J. L. Faria, J. Xu, B. Li, L. Liu, *ACS Catal.* **2022**, *12*, 9397.
[8] Z.-Y. Yu, Y. Duan, X.-Y. Feng, X. Yu, M.-R. Gao, S.-H. Yu, *Adv. Mater.* **2021**, *33*, 2007100.
[9] S. van Renssen, *Nat. Clim. Change* **2020**, *10*, 799.
[10] O. Schmidt, A. Gambhir, I. Staffell, A. D. Hawkes, J. Nelson, S. Few, *Int. J. Hydrogen Energy* **2017**, *42*, 30470.
[11] J. Guo, Y. Zheng, Z. Hu, C. Zheng, J. Mao, K. Du, M. Jaroniec, S.-Z. Qiao, T. Ling, *Nat. Energy* **2023**, *8*, 1418.
[12] M. A. Khan, T. Al-Attas, S. Roy, M. M. Rahman, N. Ghaffour, V. Thangadurai, S. Larter, J. Hu, P. M. Ajayan, M. G. Kibria, *Energy Environ. Sci.* **2021**, *14*, 4831.
[13] W. Tong, M. Forster, F. Dionigi, S. Dresp, R. Sadeghi Erami, P. Strasser, A. J. Cowan, P. Farràs, *Nat. Energy* **2020**, *5*, 367.
[14] F. Dionigi, T. Reier, Z. Pawolek, M. Gliech, P. Strasser, *ChemSusChem* **2016**, *9*, 962.
[15] Z. Yu, L. Liu, *Adv. Mater.* **2024**, *36*, 2308647.
[16] Z. Yu, C. Si, F. Sabaté, A. P. LaGrow, Z. Tai, V. M. Diaconescu, L. Simonelli, L. Meng, M. J. Sabater, B. Li, L. Liu, *Chem. Eng. J.* **2023**, *470*, 144050.
[17] H. Tan, Z. Yu, C. Zhang, F. Lin, S. Ma, H. Huang, H. Li, D. Xiong, L. Liu, *Energy Environ. Sci.* **2025**, *18*, 1440.
[18] Z. Yu, G. D'Olimpio, H. Huang, C.-N. Kuo, C. S. Lue, G. Nicotra, F. Lin, D. W. Boukhvalov, A. Politano, L. Liu, *Adv. Funct. Mater.* **2024**, *34*, 2403099.
[19] Z. Yu, Y. Li, V. Martin-Diaconescu, L. Simonelli, J. Ruiz Esquius, I. Amorim, A. Araujo, L. Meng, J. L. Faria, L. Liu, *Adv. Funct. Mater.* **2022**, *32*, 2206138.
[20] K. Xu, L. Liang, T. Li, M. Bao, Z. Yu, J. Wang, S. M. Thalluri, F. Lin, Q. Liu, Z. Cui, S. Song, L. Liu, *Adv. Mater.* **2024**, *36*, 2403792.
[21] X. Du, M. Tan, T. Wei, H. Kobayashi, J. Song, Z. Peng, H. Zhu, Z. Jin, R. Li, W. Liu, *Chem. Eng. J.* **2023**, *452*, 139404.
[22] Q. Mao, K. Deng, H. Yu, Y. Xu, Z. Wang, X. Li, L. Wang, H. Wang, *Adv. Funct. Mater.* **2022**, *32*, 2201081.
[23] Y. Yang, R. Zou, J. Gan, Y. Wei, Z. Chen, X. Li, S. Admassie, Y. Liu, X. Peng, *Green Chem.* **2023**, *25*, 4104.
[24] M. Zhang, J. Guan, Y. Tu, S. Chen, Y. Wang, S. Wang, L. Yu, C. Ma, D. Deng, X. Bao, *Energy Environ. Sci.* **2020**, *13*, 119.
[25] L. Zhang, Z. Wang, J. Qiu, *Adv. Mater.* **2022**, *34*, 2109321.
[26] T. Wang, X. Cao, L. Jiao, *Angew. Chem., Int. Ed.* **2022**, *61*, 202213328.
[27] Z. Xiao, C. Lu, J. Wang, Y. Qian, B. Wang, Q. Zhang, A. Tang, H. Yang, *Adv. Funct. Mater.* **2023**, *33*, 2212183.
[28] Z. Yu, D. W. Boukhvalov, H. Tan, D. Xiong, C. Feng, J. Wang, W. Wang, Y. Zhao, K. Xu, W. Su, X. Xiang, F. Lin, H. Huang, F. Zhang, L. Zhang, L. Meng, L. Liu, *Chem. Eng. J.* **2024**, *494*, 153094.
[29] S. Zhang, Q. Zhou, Z. Shen, X. Jin, Y. Zhang, M. Shi, J. Zhou, J. Liu, Z. Lu, Y.-N. Zhou, H. Zhang, *Adv. Funct. Mater.* **2021**, *31*, 2101922.
[30] X. Teng, K. Shi, L. Chen, J. Shi, *Angew. Chem., Int. Ed.* **2024**, *63*, 202318585.
[31] T. Li, Y. Yao, B. H. Ko, Z. Huang, Q. Dong, J. Gao, W. Chen, J. Li, S. Li, X. Wang, R. Shahbazian-Yassar, F. Jiao, L. Hu, *Adv. Funct. Mater.* **2021**, *31*, 2010561.
[32] Y. Yao, Z. Huang, P. Xie, S. D. Lacey, R. J. Jacob, H. Xie, F. Chen, A. Nie, T. Pu, M. Rehwoldt, D. Yu, M. R. Zachariah, C. Wang, R. Shahbazian-Yassar, J. Li, L. Hu, *Science* **2018**, *359*, 1489.
[33] Y. Shimomura, M. Kojima, S. Saito, *J. Phys. Soc. Jpn.* **1956**, *11*, 1136.
[34] Y. Luo, L. Tang, U. Khan, Q. Yu, H.-M. Cheng, X. Zou, B. Liu, *Nat. Commun.* **2019**, *10*, 269.
[35] M.-X. Qiao, Y. Zhang, L.-F. Zhai, M. Sun, *Chem. Eng. J.* **2018**, *344*, 410.
[36] M. Kumar, T. C. Nagaiah, *J. Mater. Chem. A* **2022**, *10*, 7048.
[37] R. Steudel, T. Chivers, *Chem. Soc. Rev.* **2019**, *48*, 3279.
[38] M. Hagen, P. Schiffels, M. Hammer, S. Dörfler, J. Tübke, M. J. Hoffmann, H. Althues, S. Kaskel, *J. Electrochem. Soc.* **2013**, *160*, A1205.
[39] D. He, P. Yang, K. Yang, J. Qiu, Z. Wang, *Adv. Funct. Mater.* **2024**, *34*, 2407601.
[40] M. F. Lagadec, A. Grimaud, *Nat. Mater.* **2020**, *19*, 1140.
[41] B. Ravel, M. Newville, *J. Synchrotron Radiat.* **2005**, *12*, 537.
[42] C. C. L. McCrory, S. Jung, I. M. Ferrer, S. M. Chatman, J. C. Peters, T. F. Jaramillo, *J. Am. Chem. Soc.* **2015**, *137*, 4347.